A thalamic circuit mechanism for stress-dependent modulation of REM sleep

Aletta Magyar[1,2,3], Péter Berki[1,3], Sándor Borbély[1], Boglárka Barsy[1,2], Anna Virág Bakacsi[1,2,3], Magor L Lőrincz[4], Ferenc Mátyás[1,2,5]

1. Institute of Experimental Medicine, Budapest, Hungary;

2. Institute of Cognitive Neuroscience and Psychology, Research Centre for Natural Sciences, Budapest, Hungary;

3. János Szentágothai Doctoral School of Neurosciences, Semmelweis University, Budapest, Hungary;

4. Department of Physiology, University of Szeged, Szeged, Hungary;

5. Department of Anatomy and Histology, University of Veterinary Medicine, Budapest, Hungary

Corresponding author: Ferenc Mátyás (matyasf@koki.hu).

Abstract

Rapid eye movement (REM) sleep is stress-sensitive and linked to cognitive processes in the prefrontal cortex. Yet, the neuronal mechanisms connecting stress, REM sleep and cortical operations remain unclear. Here, we reveal that prefrontal cortical- and nucleus accumbens-projecting paraventricular thalamic neurons (PVT_{NAc}) exhibit sleep-stage dependent activity and modulate cortical REM oscillation in response to stress. We found that PVT_{NAc} bidirectionally modulate the REM-promoting medullary GABAergic signal, and thus, cortical theta oscillation during REM sleep in an activity-dependent manner, along with the excitation-inhibition balance observed during natural sleep stage transitions. While acute stress enhances REM sleep, repeated stress suppresses it through progressively increased PVT_{NAc} activation. Notably, acute and chronic stimulation of PVT_{NAc} recapitulates stress-induced bidirectional

changes in REM sleep. Thus, PVT_{NAc} neurons, by integrating stress and REM signals into forebrain activity, dynamically shape sleep architecture. Persistent elevation in this pathway disrupts REM sleep, thereby providing a mechanism through which stress alters prefrontal cortical processing and, ultimately, cognitive functions.

Main

Neuronal oscillations of cortical networks are fundamental in regulating brain states and influencing cognitive functions. In particular, Rapid Eye Movement (REM) sleep has been linked to key cognitive processes such as memory formation and problem solving, in both human and mice[3,11–14]. Studies have demonstrated a direct causal relationship between sleep rhythms, especially REM sleep, and cognitive performance. Disruption of REM sleep is implicated in various psychiatric disorders including post-traumatic stress disorder, anxiety disorders, cognitive impairments in Parkinson's disease as well as Alzheimer's disease [11,15–18]. These findings suggest that cortical REM rhythms could serve as valuable biomarkers for the development of such pathologies.

The prefrontal cortex (PFC) plays an essential role in regulating sleep-dependent cognitive processes[19–21] and is also crucial for mediating maladaptive stress responses[22,23], often marked by alterations in REM sleep[5]. Recent evidence highlights the critical involvement of PFC in regulation of REM sleep[24], suggesting that the PFC is central to the 'stress-REM sleep-cognition' axis. However, despite its importance, the precise mechanisms underlying the regulation of cortical REM oscillations, and how these rhythms contribute to the stress-sensitivity of REM sleep, remain poorly understood.

Cortical functions related to sleep and cognition are strongly influenced by its thalamic inputs[25–27], particularly from the midline thalamic paraventricular nucleus (PVT)[28–30]. The PVT has extensive projections to the PFC and is important in encoding salience, arousal and homeostatic signals within the forebrain[29–33], and also in shaping behavioral responses to stress[10,34–37]. Given these functions, we hypothesize that the PVT may regulate REM oscillation in a stress-dependent manner, linking cortical REM sleep patterns to the stress response.

PVT neurons with sleep-stage dependent activity

First, we ought to test whether PVT neurons exhibit sleep-state dependent activity pattern. To target PVT neurons, we used the calretinin (CR, '*Calb2*')-Cre mice, as the majority of PFC-projecting PVT cells express calretinin[29]. We injected the PVT of CR-Cre mice with a Cre-dependent recombinant adeno-associated virus (AAV) expressing Channelrhodopsin 2 (ChR2). Three weeks later, we implanted optrodes-tetrode configured wire bundles surrounding an optical fiber to record the activity of optogenetically identified PVT cells during natural home-cage sleep. Simultaneously, EEG and EMG electrodes were placed above the frontal cortex and in the neck muscle to classify brain states (awake, non-REM, REM) based on theta (4-8 Hz for REM) and delta (1-4 Hz for NREM) – oscillations and EMG signals (Fig. 1a,b). Analysis of identified PVT_{CR+} cells (N = 34 cells, n = 3 mice) revealed diverse state-dependent activity modulations. At population level, PVT_{CR+} neurons fired at a significantly higher rate during REM sleep compared to NREM sleep (Fig. 1c and Extended Data Fig. 1a) with the most pronounced increase occurring at NREM-to-REM transitions (Fig. 1c and Extended Data Fig. 1b,c). A negative correlation was also observed between the baseline firing rate and REM-induced firing rate changes, indicating that neurons with lower baseline firing rates exhibited greater REM-associated activation (Fig. 1d).

PVT transmits VLM_{GABA} signal to the PFC

To identify upstream sources regulating PVT activity and cortical REM states we examined the ventrolateral medullary GABAergic (VLM_{GABA}) input to PVT, as this population has been implicated in REM sleep regulation[7,8]. We injected a Cre-dependent eYFP vector into the VLM of vGAT-Cre mice (n = 3 mice; Fig. 2a) and observed that VLM_{GABA} axons project topographically to the middle-posterior PVT with the strongest input localized to this region (Fig. 2b,c).

To determine how VLM_{GABA} influences PVT and, in turn, PFC activity and cortical oscillations, we virally expressed NpHR3.0 in VLM_{GABA} cells of vGAT-Cre mice (n = 7) and performed simultaneous in vivo extracellular recordings from PVT and PFC while optogenetically inhibiting VLM_{GABA}-to-PVT terminals under anesthesia (Fig. 2d and Extended Data Fig. 1d). This configuration allowed us to perform cell-type-selective cortical and thalamic recordings over extended periods and differentiate local field potential signal (LFP) from superficial (layers 1-3) and deep (layers 5-6) PFC regions, given that sleep oscillations exhibit laminar profiles, with higher REM associated cortical activity in superficial layers[9,38–40]. Consistent with the heterogeneous sleep-state-dependent activity of PVT cells (Fig. 1 and Extended Data Fig. 1e,f), inhibition of VLM_{GABA} input produced diverse firing rate changes in individual PVT cells, particularly during REM-like high-theta periods (N=95 cells, n = 7 mice; Fig. 2e). Notably, VLM_{GABA} modulated cells (PVT_{MOD}; N = 68) exhibited lower baseline firing rates than non-modulated neurons (PVT_{MOD}, N = 68: 0.74±0.85 Hz; PVT_{NON}, N = 27: 1.85±1.97 Hz), and only PVT_{MOD} neurons showed increased activity during NREM-to-REM transitions (Fig. 2f,g and Extended Data Fig. 2a,b).

Moreover, the REM-associated firing rate changes correlated with the baseline activity of PVT_{MOD} but not the PVT_{NON} neurons (Fig. 2h). Optogenetic silencing of VLM_{GABA} input, both non-selectively and specifically during REM-like states, disrupted ongoing theta oscillations in the superficial PFC (Fig. 2i,j and Extended Data Fig. 2c-h). Notably, REM-associated silencing had a stronger theta-suppressive effect in 6 out of 7 mice (Extended Data Fig. 2i), suggesting that a subpopulation of PVT neurons is under REM-related VLM_{GABA} control and influences sleep oscillations in a VLM_{GABA}-dependent manner.

In parallel with PVT and theta oscillation changes, prefrontal cortical interneurons (INs) and principal neurons (PNs) were also modulated by the inhibition of VLM_{GABA}-to-PVT terminals. A larger proportion of INs and PNs exhibited activity changes when optogenetic silencing

occurred during REM-like states compared to all trials (Fig. 2k). Further classification of INs based on their electrophysiological properties (Extended Data Fig. 3a-d) revealed that fast-spiking (FS) and non-fast-spiking (NFS) neurons responded divergently. FS neurons decreased while NFS neurons increased their activity[9] upon optogenetic silencing of VLM_{GABA}-to-PVT inputs, coinciding with reduced theta oscillation (Fig. 2l and Extended Data Fig. 3e-g). These findings suggest that the VLM_{GABA} input exerts an inhibitory influence on a subset of PVT neurons, which in turn modulates REM states via the PFC network.

PVT_{NAc} neurons mediate REM sleep via VLM_{GABA}

A subset of low firing PVT neurons mediates VLM-driven theta oscillatory changes during sleep. The PVT-to-nucleus accumbens (PVT_{NAc}) and PVT-to-amygdala (PVT_{AMY}) pathways represent the two largest PVT subpopulations, each with distinct connectivity and functions[29,31,41,42]. To determine whether either group is under VLM_{GABA} control and can exert a laminar-selective influence on PFC and REM sleep, we employed multiple approaches.

First, we retrogradely labeled PVT_{NAc} or PVT_{AMY} neurons using rgAAV-eYFP while VLM_{GABA} cells of vGAT-Cre mice were transduced with ChR2 carrying AAV. After 8–10 weeks, we conducted acute slice electrophysiology on coronal slices from the middle-posterior PVT (Fig. 3a,b). Optogenetic activation of VLM_{GABA}-to-PVT fibers evoked $GABA_A$ mediated inhibitory postsynaptic potentials (eIPSCs) in both PVT_{NAc} and PVT_{AMY} neurons (Fig. 3c). However, eIPSCs amplitudes were significantly larger than spontaneous IPSCs in PVT_{NAc} but not PVT_{AMY} neurons (Fig. 3d). Additionally, PVT_{NAc} neurons exhibited stronger and more reliable inhibitory responses than PVT_{AMY} neurons across all stimulation frequencies (Fig. 3e,f). While VLM_{GABA}-to-PVT_{AMY} synapses displayed short-term depression at 5/10/20 Hz, VLM_{GABA}-to-PVT_{NAc} synapses maintained stable transmission (Fig. 3e,f), suggesting that PVT_{NAc} neurons more efficiently relay VLM_{GABA} inputs.

To reveal PVT_{NAc} involvement in REM sleep, we used retroanterograde labeling[29] in CR-Cre mice to express ChR2 in either PVT_{NAc} or PVT_{AMY} neurons, then recorded their firing rates across natural sleep stages (Extended Data Fig. 4a-g and Extended Data Fig. 5a). PVT_{NAc} neurons had lower baseline activity and stronger REM modulation compared to PVT_{AMY} neurons (Fig. 3h and Extended Data Fig. 5b,c). Only PVT_{NAc} neurons increased firing at the NREM-to-REM transition (Fig. 3i and Extended Data Fig. 5d) and showed a negative correlation between baseline activity and REM-induced firing changes (Fig. 3j) resembling VLM_{GABA}-modulated PVT neurons. Furthermore, PVT_{NAc} firing was phase-locked to the ascending theta cycle, whereas PVT_{AMY} firing aligned with the descending phase, suggesting a PVT_{NAc}-mediated role in theta oscillations (Fig. 3k).

These findings establish PVT_{NAc} as the key PVT subpopulation transmitting VLM_{GABA} input to the PFC and promoting cortical REM sleep.

To directly test the impact of PVT_{NAc} and PVT_{AMY} neurons on REM sleep, we optogenetically activated these neurons at two different frequencies during natural sleep (Methods). Since PVT_{NAc} activity naturally rises to ∼1 Hz before NREM-to-REM transitions (Fig. 3i and Extended Data Fig. 5d) and sustains this frequency throughout REM, we applied a 1 Hz stimulation protocol in addition to a 10 Hz protocol as activity of PVT cells were shown to reach this frequency[29]. 1 Hz PVT_{NAc} activation (n = 7 mice) enhanced REM sleep by increasing theta power and duration (Fig. 3l,m and Extended Data Fig. 5e,g). In contrast, 10 Hz PVT_{NAc} activation suppressed REM-associated theta oscillations (Fig. 3n,o and Extended Data Fig. 5f,h). These effects were absent in PVT_{AMY} (n = 8) and PVT_{YFP} mice (n =3; Fig. 3l-o and Extended Data Fig. 5e-j) indicating that PVT_{NAc} exerts bidirectional control over REM sleep in an activity-dependent manner.

Activity-dependent PVT_{NAc} effects on PFC circuit

We next examined whether frequency-dependent activation of PVT_{NAc} – which bidirectionally modulates theta oscillations – contributes to REM sleep–specific prefrontal reorganization[9] (Fig. 2l). To monitor PN, FS and NFS neurons, we combined acute *in vivo* extracellular LFP recordings with single-unit activity measurements during optogenetic stimulation of PVT_{NAc}, alongside PVT_{AMY} for comparison. Antidromic activation of PVT_{NAc} and PVT_{AMY} neurons was robust (Extended Data Fig. 6a-e) and induced distinct, layer-specific effects in the PFC, consistent with their projection patterns (Fig. 4a,b and Extended Data Fig. 6f-i). PVT_{NAc} activation engaged a larger fraction of PFC neurons and resulted in a better signal-to-noise ratio in superficial layers compared to PVT_{AMY} (Fig. 4c-h).

Notably, in the anesthetized condition, 1 Hz and 10 Hz stimulation of PVT_{NAc} (Extended Data Fig. 7a,b) elicited opposing changes in PFC theta power (increased and decreased; respectively) mirroring the effects observed in natural sleep conditions (Fig 3). Similar LFP dynamics were detected in the primary somatosensory cortex (Extended Data Fig. 7c,d), indicating that PVT_{NAc}—but not PVT_{AMY}—can orchestrate global theta oscillations changes during sleep.
When 1 Hz PVT_{NAc} activation enhanced theta power in PFC, FS neuron activity increased, while NFS and PN activity decreased. The opposite occurred with 10 Hz stimulation, which suppressed theta power (Fig. 4i and Extended Data Fig. 8a). Similar microcircuit reorganization was observed during spontaneous sleep state transitions: from low-to-high theta (as in NREM-to-REM) and high-theta-to-desynchronized states (as in REM-to wake transitions; Fig. 4j and Extended Data Fig. 8b). These findings indicate that PVT_{NAc}, but not PVT_{AMY} (Fig. 4k and Extended Data Fig. 8c), selectively shapes PFC microcircuit dynamics underlying theta oscillation in an activity-dependent manner.

PVT_{NAc} bidirectionally modulate the VLM_{GABA} effects on theta oscillation

The above results collectively suggest that PVT_{NAc} is able to maintain or suppress the VLM_{GABA}

input-mediated effects on theta oscillation. To directly verify this, PVT_{CR+} and VLM_{GABA} were transduced with ChR2 carrying AAVs in CR-Cre/vGAT-FLPO mice and, then, antidromic activation of PVT_{NAc} and orthodromic activation of VLM_{GABA} neurons were simultaneously applied (Fig. 5a). Optogenetic activation of VLM_{GABA} only changed the firing rate of the photo-identified PVT_{NAc} but not the un-identified neurons (PVT_{UN}; Fig. 5b). Notably, PVT_{NAc} activity was actually increased to ~1 Hz. This elevation was further increased when VLM_{GABA} stimulation was paired with 1 Hz PVT_{NAc} activation, and even further, when it was paired with 10 Hz thalamic stimulation (Fig. 5c). This progressively elevated PVT_{NAc} activity bidirectionally modulated the theta rhythm-promoting VLM_{GABA} effect: while 1 Hz PVT_{NAc} activation maintained and even prolonged, 10 Hz thalamic stimulation suppressed the power of theta oscillation (Fig. 5d). These results confirm that, despite the ongoing VLM_{GABA} signaling, PVT_{NAc} – in an activity-dependent manner – can enhance or suppress REM-associated PFC theta oscillation.

Stress-induced REM sleep modulation by PVT_{NAc} neurons

Stress exerts bidirectional effects on REM sleep: while acute stress transiently enhances REM as an adaptive response, chronic or intense stress suppresses it[6,43]. Having identified PVT_{NAc} neurons as key mediators of VLM_{GABA}-to-PFC signaling in physiological regulation of REM sleep, we next investigated whether this population also contributes to stress-induced modulation of REM sleep.

We employed a 4-day restraint stress paradigm, allowing us to monitor the activity of the optogenetically identified PVT cells during both acute and chronic stress as well as REM sleep. Following a habituation day (R0), mice underwent 3 days of restraint stress (R1-3), with R1 representing acute stress and R2-3 modelling chronic stress (Fig. 6a). Throughout the experiment, frontal cortical EEG, EMG, and thalamic single unit recordings were conducted during habituation/restraint and the subsequent 6-hour post restraint sleep periods (PRS0-3).

Mice (n=6 mice) exhibited biphasic REM sleep modulation: REM sleep increased following acute stress (R1, PRS1), but was progressively suppressed with repeated restraint (R2-3, PRS2-3). By the third day, REM sleep duration was significantly reduced compared to baseline (PRS0; Fig. 6b and Extended Data Fig. 9a). Concurrently, PVT_{NAc} neurons (N=11 cells; n=3 mice) showed increased firing during both the restraint and post-restraint sleep periods, with some cells reaching mean firing rates of 10 Hz, which response was absent in PVT_{AMY} neurons (N=9 cells, n=3 mice; Fig. 6c-e and Extended Data Fig. 9b,c).

To establish a causal link between the progressive increase in PVT_{NAc} activity and bidirectional REM sleep modulation, we optogenetically activated PVT_{NAc} during sleep across multiple days while monitoring frontal EEG activity (n = 7 mice; Fig. 6f; Methods). Control groups included mice expressing ChR2 in PVT_{AMY} (n = 8) and YFP in PVT (n = 3). Despite individual variability, PVT_{NAc} stimulation produced bidirectional REM modulation, mirroring the effects of restraint stress: stimulation on the first two days (S1-2) increased REM sleep, resembling the acute response, whereas continued stimulation (S3-6) progressively suppressed REM sleep, similar to chronic stress (Fig. 6g and Extended Data Fig. 9b). PVT_{NAc} firing also exhibited a progressive increase in non-stimulated periods, paralleling the impact of restraint stress (Fig. 6h-i). In contrast, PVT_{AMY}-stimulated and YFP expressing mice showed no REM alterations (Fig. 6g and Extended Data Fig. 9e,f). The comparable REM sleep dynamics induced by restraint and PVT_{NAc} activation (Fig. 6e,i and Extended Data Fig. 9g) indicate that progressive PVT_{NAc} recruitment mediates stress-dependent REM sleep plasticity.

Finally, Rabies-mediated monosynaptic retrograde tracing revealed that PVT_{NAc} neurons receive a broader array of brain-wide inputs than PVT_{AMY}, including projections from stress-sensitive and REM-regulating hypothalamic, mesencephalic and brainstem nuclei (Extended Data Fig. 10a-h). These findings position PVT_{NAc} as a central hub for integrating stress signals and modulating cortical circuits accordingly during sleep (Fig. 6j).

Discussion

Understanding the network mechanism behind stress-induced REM sleep modulation in the PFC has broad implications for understanding how daily stressors can influence cognitive performance on subsequent days. Our findings reveal a convergence of inputs that regulate REM sleep rhythm, specifically from VLM_{GABA}[7,8] (Figs. 2,3 and 5), which generates the REM rhythm, and from brain-wide stress-signal carrying pathways[44,45] onto the PVT_{NAc} population (Extended Data Fig. 10). We further demonstrate that PVT_{NAc} activity increases progressively from acute to chronic stress, driving bidirectional changes in REM sleep. Acute stress results in a REM rebound effect, whereas repeated stress exposure leads to elevated PVT_{NAc} activity and REM disruption (Fig. 6). In an activity-dependent manner, PVT_{NAc} also maintains or suppresses the effect of VLM_{GABA} signalling and drives the shift in the inhibitory/excitatory balance within the PFC which, in turn, is manifested as bidirectional changes in REM-associated theta oscillation during sleep (Figs. 4,5). Ultimately, stress-driven neuronal reorganization modulated by PVT_{NAc} activity may also lead to persistent changes within frontal cortical structure and function[46–49].

In addition to the VLM_{GABA} input, the PVT also integrates a variety of subcortical inputs essential for fine-tuning REM rhythm regulation. These inputs, originating from the locus coeruleus[10,50], lateral hypothalamus[51], tegmental/pontine area[52] and preoptic area[53] (Extended Data Fig. 10), all converge at the level of the PVT_{NAc}, enabling it to act as a crucial hub in regulating cortical theta oscillations during REM sleep.

Depending on the strength of these inputs, PVT_{NAc} activity can either promote or suppress cortical theta oscillation by altering the activity of PFC inhibitory circuits. Notably, our findings also suggest that the intensity of daily stressors plays a pivotal role in determining how these signals interact within the PVT and the PFC. Acute or mild stress can boost FS-based feed-

forward inhibition and promote REM; whereas chronic or intense stress results in overactivation of PVT_{NAc} shifting the balance toward NFS-based inhibition and REM suppression[9,54,55]. Thus, PVT_{NAc} is uniquely positioned to modulate cortical REM sleep in a stress-dependent manner, driving opposite effects on theta oscillations depending on the nature and duration of the stressor.

Both REM-facilitation (by acute stress) and REM-suppression (by chronic or strong stress) require long-lasting neuromodulatory signals that contribute to persistent changes in sleep and cortical functions. Notably, nitric oxide (NO), a key neuromodulator involved in sleep-wake regulation emerges as a crucial mediator of stress-induced bidirectional REM sleep alterations[56,57]. Acute stress has been shown to decrease cortical NO levels, whereas repeated stress elevates them[58]. Given that PVT_{NAc} cells express NO synthetizing enzymes (Extended Fig. 11), the NO released from these cells may play a central role in shaping the activity-dependent shifts in the PFC that underpin REM sleep modulation.

In addition, corticotrophin-releasing hormone (CRH), another stress-related neuromodulator, has been implicated in regulating sleep[59,60], with acute stress causing an increase in CRH that contributes to REM sleep rebound[61,62]. As PVT_{NAc} cells express CRH[63], their elevated activation triggered CRH release may also influence cortical activity and drive REM sleep changes. Together, these suggest that the dynamic interplay between PVT_{NAc} NO and CRH is central to the modulation of REM sleep in response to stress.

Our findings indicate that PVT_{NAc} provides a unique upstream contribution to the cortex by integrating stress and REM-related signals. By shaping the activity and rhythm of key cortical cell types, PVT_{NAc} influences REM sleep and helps to organize state-driven emotional and cognitive processes.

References

1. Harrington, M. O. *et al.* Memory control deficits in the sleep-deprived human brain. *Proc. Natl. Acad. Sci.* **122,** (2025).

2. Muzur, A., Pace-Schott, E. F. & Hobson, J. A. The prefrontal cortex in sleep. *Trends Cogn. Sci.* **6,** 475–481 (2002).

3. Nishida, M., Pearsall, J., Buckner, R. L. & Walker, M. P. REM Sleep, Prefrontal Theta, and the Consolidation of Human Emotional Memory. *Cereb. Cortex* **19,** 1158–1166 (2009).

4. Menz, M. M., Rihm, J. S. & Büchel, C. REM Sleep Is Causal to Successful Consolidation of Dangerous and Safety Stimuli and Reduces Return of Fear after Extinction. *J. Neurosci.* **36,** 2148–2160 (2016).

5. Nollet, M. *et al.* REM sleep's unique associations with corticosterone regulation, apoptotic pathways, and behavior in chronic stress in mice. *Proc. Natl. Acad. Sci.* **116,** 2733–2742 (2019).

6. Kim, E. J. & Dimsdale, J. E. The effect of psychosocial stress on sleep: A review of polysomnographic evidence. *Behav. Sleep Med.* **5,** 256–278 (2007).

7. Weber, F. *et al.* Control of REM sleep by ventral medulla GABAergic neurons. *Nature* **526,** 435–438 (2015).

8. Valencia Garcia, S. *et al.* Ventromedial medulla inhibitory neuron inactivation induces REM sleep without atonia and REM sleep behavior disorder. *Nat. Commun.* **9,** 504 (2018).

9. Aime, M. *et al.* Paradoxical somatodendritic decoupling supports cortical plasticity

during REM sleep. *Science (80-.).* **376,** 724–730 (2022).

10. Beas, B. S. *et al.* The locus coeruleus drives disinhibition in the midline thalamus via a dopaminergic mechanism. *Nature Neuroscience* (2018). doi:10.1038/s41593-018-0167-4

11. della Monica, C., Johnsen, S., Atzori, G., Groeger, J. A. & Dijk, D.-J. Rapid Eye Movement Sleep, Sleep Continuity and Slow Wave Sleep as Predictors of Cognition, Mood, and Subjective Sleep Quality in Healthy Men and Women, Aged 20–84 Years. *Front. Psychiatry* **9,** (2018).

12. Lewis, P. A., Knoblich, G. & Poe, G. How Memory Replay in Sleep Boosts Creative Problem-Solving. *Trends in Cognitive Sciences* **22,** 491–503 (2018).

13. Li, W., Ma, L., Yang, G. & Gan, W.-B. REM sleep selectively prunes and maintains new synapses in development and learning. *Nat. Neurosci.* **20,** 427–437 (2017).

14. Walker, M. P., Liston, C., Hobson, J. A. & Stickgold, R. Cognitive flexibility across the sleep–wake cycle: REM-sleep enhancement of anagram problem solving. *Cogn. Brain Res.* **14,** 317–324 (2002).

15. Nir, Y. *et al.* Selective neuronal lapses precede human cognitive lapses following sleep deprivation. *Nat. Med.* **23,** 1474–1480 (2017).

16. Wulff, K., Gatti, S., Wettstein, J. G. & Foster, R. G. Sleep and circadian rhythm disruption in psychiatric and neurodegenerative disease. *Nat. Rev. Neurosci.* **11,** 589–599 (2010).

17. Jozwiak, N. *et al.* REM Sleep Behavior Disorder and Cognitive Impairment in Parkinson’s Disease. *Sleep* **40,** (2017).

18. Katsuki, F., Gerashchenko, D. & Brown, R. E. Alterations of sleep oscillations in Alzheimer's disease: A potential role for GABAergic neurons in the cortex, hippocampus, and thalamus. *Brain Res. Bull.* **187,** 181–198 (2022).

19. Horne, J. A. Human Sleep, Sleep Loss and Behaviour. *Br. J. Psychiatry* **162,** 413–419 (1993).

20. Durmer, J. S. & Dinges, D. F. Neurocognitive Consequences of Sleep Deprivation. *Semin. Neurol.* **25,** 117–129 (2005).

21. Verweij, I. M. *et al.* Sleep deprivation leads to a loss of functional connectivity in frontal brain regions. *BMC Neurosci.* **15,** 88 (2014).

22. Arnsten, A. F. T. Stress signalling pathways that impair prefrontal cortex structure and function. *Nat. Rev. Neurosci.* **10,** 410–422 (2009).

23. Cerqueira, J. J., Mailliet, F., Almeida, O. F. X., Jay, T. M. & Sousa, N. The Prefrontal Cortex as a Key Target of the Maladaptive Response to Stress. *J. Neurosci.* **27,** 2781–2787 (2007).

24. Hong, J., Lozano, D. E., Beier, K. T., Chung, S. & Weber, F. Prefrontal cortical regulation of REM sleep. *Nat. Neurosci.* **26,** 1820–1832 (2023).

25. Steriade, M., McCormick, D. A. & Sejnowski, T. J. Thalamocortical oscillations in the sleeping and aroused brain. *Science* **262,** 679–685 (1993).

26. Sherman SM, G. R. *Exploring the thalamus and its role in cortical function. 2nd ed.* (MIT Press, 2006).

27. Shine, J. M., Lewis, L. D., Garrett, D. D. & Hwang, K. The impact of the human thalamus on brain-wide information processing. *Nat. Rev. Neurosci.* **24,** 416–430

(2023).

28. Vertes, R. P., Linley, S. B. & Hoover, W. B. Limbic circuitry of the midline thalamus. *Neuroscience and Biobehavioral Reviews* **54,** 89–107 (2015).

29. Mátyás, F. *et al.* A highly collateralized thalamic cell type with arousal-predicting activity serves as a key hub for graded state transitions in the forebrain. *Nat. Neurosci.* **21,** 1551–1562 (2018).

30. Ren, S. *et al.* The paraventricular thalamus is a critical thalamic area for wakefulness. *Science (80-.).* **362,** 429–434 (2018).

31. Ma, J. *et al.* Divergent projections of the paraventricular nucleus of the thalamus mediate the selection of passive and active defensive behaviors. *Nat. Neurosci.* **24,** 1429–1440 (2021).

32. Zhu, Y. *et al.* Dynamic salience processing in paraventricular thalamus gates associative learning. *Science (80-.).* **362,** 423–429 (2018).

33. Colavito, V., Tesoriero, C., Wirtu, A. T., Grassi-Zucconi, G. & Bentivoglio, M. Limbic thalamus and state-dependent behavior: The paraventricular nucleus of the thalamic midline as a node in circadian timing and sleep/wake-regulatory networks. *Neurosci. Biobehav. Rev.* **54,** 3–17 (2015).

34. Herman, J. P. Neural control of chronic stress adaptation. *Front. Behav. Neurosci.* **7,** (2013).

35. Hsu, D. T., Kirouac, G. J., Zubieta, J.-K. & Bhatnagar, S. Contributions of the paraventricular thalamic nucleus in the regulation of stress, motivation, and mood. *Front. Behav. Neurosci.* **8,** (2014).

36. Pliota, P. *et al.* Stress peptides sensitize fear circuitry to promote passive coping. *Mol. Psychiatry* **25,** 428–441 (2020).

37. Jász, A. *et al.* Persistently increased post-stress activity of paraventricular thalamic neurons is essential for the emergence of stress-induced alterations in behaviour. *PLOS Biol.* **23,** e3002962 (2025).

38. Csercsa, R. *et al.* Laminar analysis of slow wave activity in humans. *Brain* **133,** 2814–2829 (2010).

39. Funk, C. M., Honjoh, S., Rodriguez, A. V., Cirelli, C. & Tononi, G. Local Slow Waves in Superficial Layers of Primary Cortical Areas during REM Sleep. *Curr. Biol.* **26,** 396–403 (2016).

40. Dong, Y., Li, J., Zhou, M., Du, Y. & Liu, D. Cortical regulation of two-stage rapid eye movement sleep. *Nat. Neurosci. 2022 2512* **25,** 1675–1682 (2022).

41. Dong, X., Li, S. & Kirouac, G. J. Collateralization of projections from the paraventricular nucleus of the thalamus to the nucleus accumbens, bed nucleus of the stria terminalis, and central nucleus of the amygdala. *Brain Structure and Function* 1–17 (2017). doi:10.1007/s00429-017-1445-8

42. Aquino-Miranda, G. *et al.* Functional properties of corticothalamic circuits targeting paraventricular thalamic neurons. *Neuron* **112,** 4060–4080.e7 (2024).

43. Suchecki, D., Tiba, P. A. & Machado, R. B. REM Sleep Rebound as an Adaptive Response to Stressful Situations. *Front. Neurol.* **3,** (2012).

44. Penzo, M. A. & Gao, C. The paraventricular nucleus of the thalamus: an integrative node underlying homeostatic behavior. *Trends in Neurosciences* **44,** 538–549 (2021).

45. Kirouac, G. J. Placing the paraventricular nucleus of the thalamus within the brain circuits that control behavior. *Neuroscience and Biobehavioral Reviews* **56,** 315–329 (2015).

46. Radley, J. J. *et al.* Repeated Stress Induces Dendritic Spine Loss in the Rat Medial Prefrontal Cortex. *Cereb. Cortex* **16,** 313–320 (2006).

47. Peever, J. & Fuller, P. M. Neuroscience: A Distributed Neural Network Controls REM Sleep. *Curr. Biol.* **26,** R34–R35 (2016).

48. Zhou, Y. *et al.* REM sleep promotes experience-dependent dendritic spine elimination in the mouse cortex. *Nat. Commun.* **11,** 4819 (2020).

49. Li, W., Ma, L., Yang, G. & Gan, W. B. REM sleep selectively prunes and maintains new synapses in development and learning. *Nat. Neurosci.* **20,** 427–437 (2017).

50. Osorio-Forero, A. *et al.* Infraslow noradrenergic locus coeruleus activity fluctuations are gatekeepers of the NREM–REM sleep cycle. *Nat. Neurosci.* **28,** 84–96 (2025).

51. Jego, S. *et al.* Optogenetic identification of a rapid eye movement sleep modulatory circuit in the hypothalamus. *Nat. Neurosci.* **16,** 1637–1643 (2013).

52. Van Dort, C. J. *et al.* Optogenetic activation of cholinergic neurons in the PPT or LDT induces REM sleep. *Proc. Natl. Acad. Sci.* **112,** 584–589 (2015).

53. Kroeger, D. *et al.* Galanin neurons in the ventrolateral preoptic area promote sleep and heat loss in mice. *Nat. Commun.* **9,** 4129 (2018).

54. Perlman, G., Tanti, A. & Mechawar, N. Parvalbumin interneuron alterations in stress-related mood disorders: A systematic review. *Neurobiol. Stress* **15,** 100380 (2021).

55. Chen, C.-C., Lu, J., Yang, R., Ding, J. B. & Zuo, Y. Selective activation of

parvalbumin interneurons prevents stress-induced synapse loss and perceptual defects. *Mol. Psychiatry* **23,** 1614–1625 (2018).

56. Cespuglio, R., Amrouni, D., Meiller, A., Buguet, A. & Gautier-Sauvigné, S. Nitric oxide in the regulation of the sleep-wake states. *Sleep Med. Rev.* **16,** 265–279 (2012).

57. Kashiwagi, M. *et al.* A pontine-medullary loop crucial for REM sleep and its deficit in Parkinson's disease. *Cell* **187,** 6272–6289.e21 (2024).

58. Gądek-Michalska, A., Tadeusz, J., Rachwalska, P., Spyrka, J. & Bugajski, J. Effect of repeated restraint on homotypic stress-induced nitric oxide synthases expression in brain structures regulating HPA axis. *Pharmacol. Reports* **64,** 1381–1390 (2012).

59. Chrousos, G. P. & Gold, P. W. The concepts of stress and stress system disorders. Overview of physical and behavioral homeostasis. *JAMA* **267,** 1244–52 (1992).

60. Kimura, M. *et al.* Conditional corticotropin-releasing hormone overexpression in the mouse forebrain enhances rapid eye movement sleep. *Mol. Psychiatry* **15,** 154–165 (2010).

61. Marrosu, F., Gessa, G. L., Giagheddu, M. & Fratta, W. Corticotropin-releasing factor (CRF) increases paradoxical sleep (PS) rebound in PS-deprived rats. *Brain Res.* **515,** 315–318 (1990).

62. Steiger, A. Sleep and the hypothalamo–pituitary–adrenocortical system. *Sleep Med. Rev.* **6,** 125–138 (2002).

63. Itoga, C. A. *et al.* New viral-genetic mapping uncovers an enrichment of corticotropin-releasing hormone-expressing neuronal inputs to the nucleus accumbens from stress-related brain regions. *J. Comp. Neurol.* **527,** 2474–2487 (2019).

64. Barsy, B. *et al.* Associative and plastic thalamic signaling to the lateral amygdala controls fear behavior. *Nat. Neurosci.* **23,** 625–637 (2020).

65. Babiczky, Á. & Matyas, F. Molecular characteristics and laminar distribution of prefrontal neurons projecting to the mesolimbic system. *Elife* (2022). doi:10.7554/eLife.78813

66. Mátyás, F., Lee, J., Shin, H. S. & Acsády, L. The fear circuit of the mouse forebrain: Connections between the mediodorsal thalamus, frontal cortices and basolateral amygdala. *Eur. J. Neurosci.* **39,** 1810–1823 (2014).

67. Steriade, M. Corticothalamic resonance, states of vigilance and mentation. *Neuroscience* **101,** 243–276 (2000).

68. Rossant, C. *et al.* Spike sorting for large, dense electrode arrays. *Nat. Neurosci.* **19,** 634–641 (2016).

69. Barthó, P. *et al.* Characterization of Neocortical Principal Cells and Interneurons by Network Interactions and Extracellular Features. *J. Neurophysiol.* (2004). doi:10.1152/jn.01170.2003

70. Gentet, L. J., Avermann, M., Matyas, F., Staiger, J. F. & Petersen, C. C. H. Membrane Potential Dynamics of GABAergic Neurons in the Barrel Cortex of Behaving Mice. *Neuron* **65,** 422–435 (2010).

71. Michaiel, A. M., Parker, P. R. L. & Niell, C. M. A Hallucinogenic Serotonin-2A Receptor Agonist Reduces Visual Response Gain and Alters Temporal Dynamics in Mouse V1. *Cell Rep.* **26,** 3475–3483.e4 (2019).

72. Do-Monte, F. H., Quinõnes-Laracuente, K. & Quirk, G. J. A temporal shift in the

circuits mediating retrieval of fear memory. *Nat. 2015 5197544* **519,** 460–463 (2015).

73. Do-Monte, F. H., Minier-Toribio, A., Quiñones-Laracuente, K., Medina-Colón, E. M. & Quirk, G. J. Thalamic Regulation of Sucrose Seeking during Unexpected Reward Omission. *Neuron* **94,** 388–400.e4 (2017).

Methods

Animals

Adult (2–5 months old female and male) CR (*Calb2*)-Cre (RRID: IMSR_JAX:010774), vGAT (*Slc32a1*)-Cre and -FLPO (from The Jackson Laboratory) mice were used. We also crossbred mice to have CR-Cre/vGAT-Flpo mice for the experiments. Female mice were used only for the anatomical investigations. Animals from the same gender were group-housed in a humidity- and temperature-controlled environment. Animals were kept under standard laboratory conditions on a 12 h light/12 h dark cycle with food and water available ad libitum. The Regional and Institutional Committee of the Research Centre for Natural Sciences, the Institute of Experimental Medicine and the National Animal Research Authorities of Hungary (PE/EA/00080-4/2023) approved all procedures. After all surgeries, animals received subcutaneous Rimadyl (Carprofen, 1.4 mg/kg).

Stereotactic surgeries

Viral injection

Mice were anesthetized with ketamine–xylazine (5:1, 3× dilution, ketamine: 100 mg/kg; xylazine: 4 mg/kg) and injected with one of the following AAV vectors with Nanoliter Injector (WPI) at a rate of 1 nl s^{-1} (50-200 nL): AAV-Ef1a-DIO-ChR2-eYFP (Penn Vector Core; titer: 5×10^{12} to 1×10^{13} genome copies (GC)/ml), AAV5-EF1a-DIO-eYFP-WPRE-hGH (Penn Vector Core; titer: 5 × 1012 GC/ml), AAV-Ef1a-DIO-ChR2-mCherry (Penn Vector Core; titer: 5×10^{12} to 1×10^{13} GC/ml), AAV-DFO-ChR2-eYFP virus (titer: 1 x 10^{13} GC/ml), AAV5-EF1a-DIO-mCherry (UNC Vector Core; titer: 5.3×10^{12} GC/ml), AAV-Ef1a-DIO-eNpHR3.0-eYFP (Penn Vector Core; titer: 3×10^{13} GC/ml), AAV-CAG-FLEXFRT-ChR2-mCherry (Addgene; titer: $\geq 7 \times 10^{12}$ GC/ml) and AAVrg-CAG-GFP (Addgene; titer: 7×10^{12} GC/ml). The target regions are (with anterior–posterior, lateral and dorsal–ventral coordinates): dorsal

midline thalamus (paraventricular thalamus, PVT; −1-1.2/±0/3.2–2.8 mm (n=35 animals); amygdala (AMY; −1.8/±3.4/-3.7 mm) (n=18 animals); nucleus accumbens (NAc; +1.4/±1.1/–3.9–4.2 mm) (n=16 animals) and ventrolateral medulla (VLM; −7.3/±1.4/–5.3 mm) (n= 27 animals).

Rabies tracing

The tracing method has been used and validated earlier[64]. CR-Cre mice were injected with 100 nL of AAV2/8-hSynFLEX-TVA-p2A-eGFP-p2A-oG (4.5×1012 GC/mL) into the PVT. After 4 weeks, mice were injected with rabies(ΔG)-EnvA-mCherry (100 nL; 3.5×107 GC/mL) into the NAc or AMY (N = 3-3). Mice were perfused after 9-10 days of survival. Both the rabies (mCherry) and the AAV (eGFP) signal were amplified by immunofluorescent staining procedure (see below).

Immunohistochemistry

All anatomical data were obtained from immunohistochemically stained mouse brain slices. Firstly, the tissue blocks were cut with a VT1200S Vibratome (Leica) into 50 µm coronal sections. Free-floating brain sections were intensively washed (5 times for 10 min) with 0.1 M PB. During immunohistochemical processing, all antibodies were diluted in 0.1 M PB. For high-quality fluorescent labeling, sections were treated with a blocking solution containing 10% normal donkey serum (NDS, Sigma-Aldrich, S30-M) or normal goat serum (NGS, Vector, S-1000, RRID: AB_2336615) and 0.5% Triton-X (Sigma-Aldrich) for 30 min at room temperature (RT). In the case of electrode track analysis, sections were cryoprotected in 30% sucrose solution overnight, and freeze thawed over liquid nitrogen and then, treated with 10% normal donkey serum solution to keep the visibility of the DiI (1,1′-Dioctadecyl-3,3,3′,3′-tetramethylindocarbocyanine perchlorate; Santa Cruz Biotechnology).

Then, the sections were incubated in primary antibody solution at RT overnight or for 2–3 days (at 4 °C). The following primary antibodies were used: green fluorescent protein (GFP, chicken, Life Technology: A10262, RRID: AB_2534023; 1:2000), mCherry (rabbit, BioVision: 5993-100, RRID: AB_1975001; 1:2000), FoxP2 (mouse, Merck Millipore: MABE415, RRID: AB_2721039; 1:500; Invitrogen: MA5-31419, RRID: AB_2787055; 1:2000; rabbit, Abcam: ab16046, RRID: AB_2107107; 1:500), Calb1(rabbit, SWANT: CB38, RRID: AB_10000340; 1:2000; mouse, SWANT: 300, RRID: AB_10000347; 1:2000), PV (mouse, SWANT: PV235, RRID: AB_10000343; 1:2000), CR (mouse, SWANT: 6B3, RRID: AB_10000320; 1:2000), Ctip2 (rat, Abcam: ab18465, RRID: AB_2064130; 1:500), WFS1 (rabbit, Proteintech: 26995-1-AP; RRID: AB_2880717; 1:500) and NOS (mouse, Sigma: N2280; RRID: AB_260754; 1:300). After the primary antibody incubation, the sections were treated with the following secondary IgG antibodies for fluorescent staining (1:500; 2 h at RT): Alexa 488-conjugated goat anti-chicken (GACh-A488; Molecular Probes: A11039, RRID: AB_142924), Alexa 488-conjugated donkey anti-mouse (DAM-A488; Jackson: 715-545-150, RRID: AB_2340846), Alexa 555-conjugated donkey anti-rabbit (DAR-A555; Invitrogen: A31572, RRID: AB_162543), Cy3-conjugated donkey anti-mouse (DAM-CY3; Jackson: 715-165-151, RRID: AB_2340813), Cy3-conjugated donkey anti-rabbit (DAR-CY3; Jackson: 711-165-152, RRID:AB_2307443), Alexa 594-conjugated donkey anti-rabbit (DAR-A594; Molecular Probes: A21207, RRID: AB_141637), Alexa 647-conjugated donkey anti-rabbit (DAR-A647; Jackson: 711-605-152, RRID: AB_2492288). In some cases, staining was enhanced after primary antibody incubation with biotinylated secondary antibodies (1:300; 2 h at RT), which are the followings: biotinylated goat anti-rabbit IgG (bHAR; Vector Laboratories: BA-1100, RRID: AB_2336201), biotinylated goat anti- mouse IgG (bHAM; Vector Laboratories: BA-2000, RRID: AB_2313581), Elite Avidin-Biotin Complex (eABC; Vector Laboratories: PK-6100, RRID: AB_2336819), streptavidin-conjugated green fluorescent antibodies (1:1000-

2000; 2 hr. at RT) (SA-A488; Jackson: 016-540-084, RRID: AB_2337249), streptavidin-conjugated red fluorescent antibodies (SA-CY3; Jackson: 016-160-084, RRID: AB_2337244), streptavidin-conjugated far red fluorescent antibodies (SA-A647; Jackson: 016-600-084, RRID: AB_2341101). All the fluorescent slices were mounted in Vectashield Mounting Medium (Vector Laboratories: H-1000, RRID: AB_2336789) or in Vectashield Mounting Medium with DAPI (Vector Laboratories: H-1200, RRID: AB_2336790).

Alternatively, we used DAB-Ni as a chromogen for Rabies. Sections were cryoprotected in 30% sucrose solution overnight, and freeze thawed over liquid nitrogen and then were treated with 1% H_2O_2 solution (10 min) for endogenous peroxide blocking. Next, the slices were incubated in 10% normal donkey serum (30 min, RT). After primary antibody incubation, slices were treated with biotinylated secondary antibodies (goat anti-rabbit or horse anti-goat IgG) and eABC (see above). To visualize the labeled cells, sections were developed with DAB-Ni. Sections were then dehydrated in xylol and mounted in DePex (Serva).

Identification of cortical layers

To differentiate the cortical layers in PrL and the primary somatosensory cortex (S1), we used combination of neurochemical markers[65]. The cortical layer 2/3 (L2/3) was identified by using Calb1 staining, while layer 6 (L6) was visualized with fork head box protein P2 (FoxP2) staining. Furthermore, for dissemination of the layer 5 were used Chicken ovalbumin upstream promoter transcription factor-interacting proteins 2 (Ctip2) and anti-Wolfram syndrome 1 (WFS1). The dorsoventral borders of the PrL cortex is determined by the parvalbumin (PV) immunostaining[66].

Axon density analysis

The retro-anterograde viral labelings were also amplified and the slices were counterstained for the above mentioned markers to identify the PrL cortex layers and borders. Confocal Z-stack

(slice number: 50; total thickness: 23.34-40.3 μm, PVT_{NAc}: 36.31±2.66 μm; PVT_{AMY}: 31.83±4.32 μm) images were taken with confocal microscope (Zeiss LSM 710; Zeiss ZEN 2010B SP1 Release version 6.0; Carl Zeiss Microimaging GmbH) a ×63 objective (10+x Plan Apochromat 10x/0.45 M27; 20x Plan Apochromat 20x/0.8 M27; 63x Plan Apochromat 63x/1.4 Oil DIC M27) at four different AP levels between Bregma +2.22 and +1.54 mm. The length of the retro-anterograde labelled CR+ axons were counted with a use of a custom-written Fiji macro[29] in a given region of interest (available at https://github.com/baabek/Axon-density-analyzer-ImageJ-script.git). The macro calculated axon length for each stack and the total axon length was summed up for each layers and slices in each animal. Then, the relative axon density was counted for each layers and slices (total axon length / slice volume (ROI area * interval)), and finally the relative axon density was calculated for the animal (RAD = total axon length/total volume). Furthermore, we determined the total axon distribution by layers for each animal (layer RAD/all RAD). To analyze the distribution of VLM_{GABA} axons in PVT, we used the same methods. The area of the PVT was determined by calretinin (CR) immunostaining[66]. The distribution of the anterogradely labelled VLM_{GABA} axons were counted between Bregma -0.3 and -2.1 mm in PVT.

Chronic optrode implantations

Four weeks after AAV-Ef1a-DIO-ChR2-eYFP and AAV5-EF1a-DIO-eYFP virus injections into AMY or NAC in CR-Cre mice, four custom-fabricated tungsten tetrodes (12.5 μm in diameter, California Fine Wire) were implanted into the PVT (AP/ML/DV (−1/±0.6/–2.8 mm at 10°). The tungsten electrodes were attached with a multimode optic fiber (105-μm core diameter, NA = 0.22; Thorlabs) (200–300 μm left between the optic fiber and tetrode tips), with the help of a polyimide tube (0.008 ID, Neuralynx). The electrode wires were joined to an electrode interface board (EIB-16, Neuralynx) by gold electrode contact pins (Neuralynx). The ground, reference, EMG, EEG wires (Phoenix Wire Inc.) were soldered to the appropriate

electrode interface board point. The tetrode impedances measured before the implantation at 1 kHz were kept between 240 and 750 kΩ (Intan Technologies). Ground and reference screws were implanted in parietal bone, respectively; an EMG wire was inserted into the neck muscle; an EEG screw was placed in frontal bone over PFC cortex. Finally, all pieces were secured onto the skull by multiple layers of dental acrylic (Paladur, Heraeus Kulzer) and shielded by a copper web. Mice were left for at least 4 days to recover and then, handled for several days.

In vivo electrophysiology in anesthetized preparations

In vivo recordings were performed 4–12 weeks after the viral injections (AAV-Ef1a-DIO-ChR2-eYFP or AAV-CAG-FLEXFRT-ChR2-mCherry into the PVT or AAV-Ef1a-DIO-eNpHR3.0-eYFP into the VLM) from the prelimbic cortex, primer somatosensory cortex and the paraventricular thalamus in urethane anesthetized (20 m/m % dilution; 0.005ml/1g) CR-Cre or vGAT-Cre transgenic mice. The head of the animal was fixed in a stereotaxic frame; a screw was driven into the occipital or into the left parietal bone, which served as a reference electrode. LFP activity as well as the extracellular unit activities from PrL, PVT and S1 were monitored with silicon probes (A1x16-5mm-50-703, L16; A1x32-10mm-50-177, L32; A2x16-10mm-100-500-177, BL32; A1x32-5mm-50-177, L32; Neuronexus), stained with fluorescent DiI. The wideband neural data (0.1–7500 Hz) were amplified (gain: 192×) and digitalized at 20 kHz (Intan Technologies). The electrodes were lowered into PrL (AP/ML/DV +2/–2.5/–3.5 mm/60°), into S1 cortex (AP/ML/DV –1.2/+3.2/–1, –0.8 mm/20°) and into PVT (AP/ML/DV –1.1/+1/–3.2 mm/20°).

For the ‘antidromic–orthodromic’ activation[29], the optic fibers were placed into the NAc and AMY, where the PVT_{CR+} fibers were activated, and the evoked LFP and unit responses were detected in PrL, S1 and PVT. Under these conditions, action potentials first traveled antidromically and, at a putative branching, could turn to orthodromic direction as well. The

NAc and AMY did not contain CR+ cells, which projected back to the PVT, so the thalamic stimulation was due to direct antidromic activation. In the cases of PVT somatic and VLM_{GABA}→PVT terminal manipulations, the optic fiber was placed above the PVT. For the VLM_{GABA} somatic stimulation, the optic fiber was placed above the VLM (AP/ML/DV –7.2/+3.3/–5.6/20°). Optogenetic activation consisted of 473-nm blue-light pulses (1s or 10s, 1 or 10 Hz, ~10-15 mW, Laserglow Technologies). In the case of the 1 s long activations, the stimulus was repeated 30 times and the interstimulus intervals were 60 s, while the 10 s long stimulations were repeated 10 times with 250 or 300 s interstimulus intervals. The optogenetic inhibition with NphR3.0 consisted of 532-nm green-light pulses (10s, ~15 mW). The lasers were triggered by analog signals driven by a National Instruments acquisition board (USB-6353) and Matlab. Analog trigger pulses were also delivered to the recording system and registered parallel with neural data with zero latency. After recordings, animals were transcardially perfused, and coronal sections were cut from the paraformaldehyde-fixed brains. The position of the silicon probes were verified based on DiI labeling of the electrode track. For determination of the layer specific mapping, we used different neurochemical markers (see above). Mice with incorrect virus injections or electrode positions were excluded from the analysis (N=4 mice).

In vivo electrophysiology of freely behaving mice

In vivo recordings from freely behaving CR-Cre mice were performed 4-5 days after the optrode implantation (into the PVT). EEG, EMG and extracellular PVT unit activities were monitored with optrodes and wire implantation (see previously). The wideband neural data (0.1–7500 Hz) were amplified (gain: 192×) and digitized at 20 kHz. Optogenetic tagging and activation consisted of 473-nm blue-light pulses (5 ms 0.5–1 Hz, for tagging; 10s 1 Hz; 10s 10 Hz; ~15 mW). The evoked unit responses were detected in PVT_{CR+}, PVT_{NAc} or PVT_{AMY} neurons simultaneously with the EEG and EMG signal. The PVT_{NAc} or PVT_{AMY} neurons were

transduced with ChR2 carrying AAV vectors using retro-anterograde viral injections. For optical identification, 5 ms long pulses were repeated 30 times, while the 10 s long 1 Hz and 10 Hz stimulations were repeated several times with random interstimulus intervals, which was minimum 300 s long. The behavior of mice was captured on video at 30 frames/s.

We measured the spontaneous sleep-wake transitions and sleep architecture of the PVT_{NAc} (N= 6 mice) and the PVT_{AMY} mice (N= 7 mice) for several days. Each day 10s 1 Hz and 10s 10 Hz stimulation were randomly applied.

Restraint stress

The spontaneous sleep-wake transitions and sleep architecture were measured in both light and dark phases (EEG, supplemented with EMG signal) and the activity of the PVT_{NAc} and PVT_{AMY} (N= 6 mice) cells. During the four-day experiment PVT_{NAc}=19 units and PVT_{AMY}= 20 units were followed. Only cells that could be followed through the entire stress paradigm were included in the further analysis (PVT_{NAc}=11 and PVT_{AMY}= 9). Daily measurements were merged, re-clustered, allowing reliable identification of corresponding data points. The first day served as a pre-restraint day (light-dark phase) followed by three consecutive days of restraint stress. Mice were exposed to 90 min of restraint stress in a falcon tube at the end of the light phase. Due to the tetrode implantation, a longitudinal gap was made on the top of the falcon tube. Immediately after the restraint stress, sleep architecture was measured during the first 6 h in the dark phase.

At the end of the experiments, animals were transcardially perfused, and coronal sections were cut from the paraformaldehyde-fixed brains. The position of the optrodes and EEG screw were verified with help of the electrode track.

Acute slice electrophysiology

For acute slice preparation, mice (vGAT-Cre, 3-month-old, N_{AMY}=5, N_{NAc}=4) were decapitated under deep isoflurane anesthesia. The brain was removed and placed into an ice-cold cutting solution, which had been bubbled with 95% O2–5% CO2 (carbogen gas) for at least 30 min before use. The cutting solution contained the following (in mM): *205 sucrose, 2.5 KCl, 26* $NaHCO_3$*, 0.5* $CaCl_2$*, 5* $MgCl_2$*, 1.25* NaH_2PO_4*, 10 glucose*, saturated with 95% O_2–5% CO_2. Coronal slices of 300 µm thickness were cut using a Vibratome (Leica VT1000S) and placed into an interface-type incubation chamber for recovery submerged in standard artificial cerebrospinal fluid (ACSF) containing the following (in mM): *126 NaCl, 2.5 KCl, 26* $NaHCO_3$*, 2* $CaCl_2$*, 2* $MgCl_2$*, 1.25* NaH_2PO_4*, 10 glucose*, saturated with 95% O_2–5% CO_2. During measurements, slices were transferred individually into a submerged-type recording chamber with a superfusion system allowing constantly bubbled (95% O_2–5% CO_2) ACSF to flow at a rate of 3-3.5 ml/min. The ACSF was adjusted to 300-305 mOsm. All measurements were carried out at 33 –34°C, temperature was maintained by a dual flow heater (Supertech Instruments). The pipette solution contained (in mM): 110 D-gluconic acid potassium salt, 4 NaCl, 20 HEPES, 0,1 EGTA, 10 phosphocreatine di(tris) salt, 2 ATP magnesium salt, 0.3 GTP sodium salt, pH: 7.3, 280-300 mOsm and biocytin (Sigma). Pipette resistances were 3-6 MΩ when filled with pipette solution. Visualization of slices and selection of retrogradely labelled AMY or NAc projecting PVT cells was guided by AAVrg-CAG-GFP signal (see: animals/Viral injection) and was imaged under an upright microscope (BX61WI; Olympus, Tokyo, Japan equipped with infrared-differential interference contrast optics and a UV lamp). Only cells located deeper than ~50 µm (measured from the slice surface) were targeted. All cells were recorded in voltage-clamp mode and held at -65 mV holding potential during the formation of the gigaseal. Series resistance was constantly monitored after the whole-cell configuration was established, and individual recordings taken for analysis showed stability in series resistance between a 5% margin during the whole recording. After the whole-cell configuration was

established, cells were clamped at -10 mV holding potential in order to record inhibitory postsynaptic currents (IPSCs). In order to evoke IPSCs, trains of 5*5ms laser light pulses (473 nm, calibrated to ~10 mW at slice surface, Sanctity Laser) were delivered at 1, 5, 10, and 20 Hz frequency by an optic fiber positioned above the slices. Recordings were performed with a Multiclamp 700B amplifier (Molecular Devices). Data was digitized at 20 kHz with a DAQ board (National Instruments, USB-6353). All data were processed and analyzed off-line using standard built-in functions of Python 2.7.0. environment. A threshold for IPSC peak detection was calculated for each neuron from a 2-minute-long baseline before stimulation trains. The threshold value was set to be $3*SD_{mean}$ of the signal. IPSPs were considered to be evoked (eIPSCs) if the peak was detected within the 2-10 ms range after a given stimulus on-set. Spontaneous IPSCs were detected for quantification from the 2-minute-long baseline region before stimulation trains.

Neural data processing

LFP analyses

The natural sleep and anesthetized measurements were analyzed in a similar way. The LFP/EEG/EMG signals were downsampled at 3000 Hz. The power of delta (1–4 Hz), theta (4-8 Hz), sigma/spindle activity (9–14 Hz), alpha (8–13 Hz), beta (13-30 Hz) frequency bands were differentiated[67]. For the further analysis the signals were filtered on a given frequency, thereafter were the absolute value of the filtered signals calculated, on which we performed smoothing in 100 ms window (RMS; root-means square) (**Extended Data Fig. 1c,d**). Sleep–wake states were determined by using RMS. In the natural sleep conditions, awake state was characterized by high alpha, beta activity (alpha, beta RMS) and low delta power (delta RMS) with high EMG (threshold >0.8), while sleep was characterized by low alpha and high delta activity with low EMG, and it was further subdivided into NREM and REM state. For the

further classification the EMG signal was normalized. REM was determined as a high sigma/delta (sigma/delta RMS) ratio associated, with low delta and high theta power and low EMG (threshold <0.5). NREM was determined as a low sigma/delta ratio associated with high delta power or spindle activity and low EMG (threshold <0.8). NREM sleep was not divided into further subsections. In the anaesthetized conditions, desynchronized state was characterized by high alpha, beta activity (alpha, beta RMS) and low delta power (delta RMS), while sleep was characterized by low alpha and high delta activity, and it was further subdivided into NREM-like and REM-like state. REM-like states were determined as a high sigma/delta (sigma/delta RMS) ratio associated with low delta and high theta power. NREM was determined as a low sigma/delta ratio associated with high delta power or spindle activity. All animals and measurements had a different sigma/delta RMS ratio, thus, the ratio was calculated for each trial and for each animal; the pre-stimulus ratio was compared to the measurement specific median. An 18 s time window, the baseline (sleep) period (between -20 s and -2 s), was used to determine pre-stimulus sleep stages. During spontaneous sleep architecture monitoring, the oscillation fluctuation was monitored in 5 s time windows.

The delta and theta RMS changes were calculated for the normalized signal after the optical stimulation or for the spontaneous state. The starting point of the elevated delta and theta RMS segment was determined by the time point, when the normalized signal exceeded the baseline for the first time after the stimulus, while the end point of the changes was the return of the RMS signal to baseline. The lengths of the delta and theta RMS changes (recovery-time) were given by the time period between these two points. The REM onset was given by the time when all the criteria of REM state appeared at the same time. 10s 1/10 Hz 10 mW optogenetic activations were applied to analyze changes in LFP activity (delta and theta RMS, FFT, modulation index (MI)). When the sleep was ‘light’ (the EEG was desynchronized) for longer periods, the stimulation protocol was paused. Sham stimuli were used as the control. The

starting point of a sham stimulus was the half point of the ISI. Sleep–wake states were determined in the case of the sham stimuli, too.

Under natural sleep conditions, the FFT and RMS changes were calculated for the frontal EEG signal. In anesthetized measurements, we could distinguish superficial and deep layers due to the insertion path of the extracellular electrode. Based on the distribution of the PVT_{NAc} and PVT_{AMY} fibers, as well as the location of the intertelenchephalic and corticothalamic/pyramidal track neurons in the PFC[65], layers 1, 2-3 and 5a were taken as the superficial, while layers 5b and 6 were considered as the deep territories. From each animal, one channel per superficial vs. deep layer was further analyzed. The channels were selected based on the best signal-to-noise ratio and were located at least 300 μm away from each other.

For identifying the state-dependent firing rate for PVT cells, EMG onset as an indicator for sleep/wake transition was set as described above. Awake periods were only accepted when these were preceded by a 30 s sleeping phase and were longer than 500 ms, defined as the lower limit for minimal arousal[29]. Peri-event time histograms (PSTH) were defined for each cell around the detected EMG onsets. Z-score values of the firing rates were given upon PSTH calculation for each cell to a 20 s baseline (sleep) period (between –30 s and –10 s, calculated from the onset of the EMG signal). Significant changes of the firing rates were defined upon at least two significant ($z > 1.92$, $P > 0.05$) neighboring z-score (1 s) bins in the [–10, 10]-s interval around EMG onset. Mean z-scores for PVT_{NAc} or PVT_{AMY} neurons are presented[29]. To determine the sleep state specific EMG changes, distinct calculation methods were used. Each animal and measurement had different EMG levels, thus for the EMG onset latency and duration were calculated for every trial, and for each animal; the pre-stimulus ratio was compared to the measurement specific median. If the median pre-stimulus EMG level was lower than the post-stimulus EMG level for each stimulus up to 18 s baseline (sleep) period (between –20 s and –2 s), then it was determined as an EMG onset.

Single cell analyses

The natural sleep and anesthetized measurements were analyzed in a similar way. Noise filtering by average subtraction and raw electrophysiological recordings were filtered (>500 Hz) for spike detection. Spike detection and principal-component-analysis-based automatic clustering were performed using SpikeDetekt and KlustaKwik (2019 edition) respectively[68]. Cell grouping was manually refined using KlustaViewa (2019 edition). A group of spikes was considered to be generated by a single neuron if they formed a discrete, well-isolated cluster and had an autocorrelogram with a refractory period (if average bin values of the first 1.5 ms did not reach the autocorrelogram's asymptote line). Cells were merged in those cases where units had the same autocorrelogram and a similarly shaped action potential on the same channel points to avoid enumerating the same cell more than once. Further data analyses were carried out using custom-built Matlab routines. All the presented electrophysiological data was derived from individually identified single units (clustered cells).

Putative principal neurons (glutamatergic cortical neurons) and GABAergic cortical interneurons were separated by the spike half-width, the autocorrelogram[69] and the baseline firing rate [70], which we considered as the most reliable parameters for this purpose. Based on previous data on cortical GABAergic interneurons, we distinguished fast spiking (FS) and non-fast spiking (NFS) interneurons based on their spike half-width, baseline firing rate and autocorrelogram (**Extended Data Fig. 3a-d**).

We calculated the signal-to-noise ratio to determine the strength of the evoked feed-back inhibition on the cortical signal (**Fig. 4e,h**). To define it, we calculated the variance of the evoked response between two time points: T_0 and $T_{\text{evoked MUA peak}}$. The $T_{\text{evoked MUA peak}}$ is the positive peak of the MUA for the 1s 10 Hz optical stimulation. The signal-to-noise ratio was then estimated as the mean at T_0 and $T_{\text{evoked MUA peak}}$ divided by standard deviation at T_0 and

$T_{evoked\ MUA\ peak}$. The evoked signal-to-noise ratio was calculated for the first three evoked MUA peaks, which were compared to the signal-to-noise ratio of the stage before the stimulus (-100 ms-0 ms).

Significant changes in evoked responses of PVT cells were validated with MI. MI was calculated for the firing rate (FR) from the mean PSTH of the pre period (between –10 s and 0 s) which was compared to the mean PSTH of the post period (between 0 s and +10 s). We expressed the modulation index as the ratio of firing rate: $(FR_{post} – FR_{pre})/(FR_{post} + FR_{pre})$[71]. Neurons with MI between 0.2 and 1 were considered as activated and with MI between -0.2 and -1, as inhibited. Both the activated and inhibited neurons were assigned to the modulated PVT (PVT_{MOD}) population. Based on these, neurons with MI between 0.2 and -0.2 were assumed as non-modulated cells (PVT_{NON}; **Fig. 2f-h**).

Furthermore, in the chronic data, thalamic unit activity was correlated with theta waves (phase-locking analysis in **Fig. 3k**). Based on the dominance of the distinct frequency band (delta, theta, sigma, gamma, EMG) the sleep stages were automatically scored. The different oscillations were normalized to the maximum power. REM was assigned to suprathreshold theta and subthreshold delta power, with low EMG. The sorted REM stages are cut out from the full measurement. After low-pass filtering the peaks of theta waves were defined. We have defined theta waves within a 0.18 s width value and with maximum 100-microvolt amplitude. Based on the width of waves the start and the end point of the theta waves are calculated. Using this data, sinusoidal waves were fitted and these hypothetical sinusoidal waves were phase-locked to the spiking activity of thalamic neurons.

Statistical analysis

The number of analyzed slices and number of cells are shown with N, while n represents the number of mice. Data from independent experiments or animals were pooled when it was

possible. Statistical significance was assessed using Kruskal-Wallis ANOVA with Mann–Whitney U-tests, Friedman ANOVA with Wilcoxon Matched Pairs Test, Paired t-test or Student's t-test with normality test, as well as analysis of variance (one-way ANOVA, repeated measures ANOVA) to analyze the axon density data or the electrophysiological data. Normality was tested using the Shapiro-Wilk test. Pearson's $\chi 2$ tests were used to compare the distribution of the responsive cortical cells. Post hoc test is used for ANOVA analysis (Fisher LSD or Bonferroni Correction). For correlation analysis Kendall's τ coefficient was used to measure the ordinal association between two measured quantities. Statistical analysis was performed using JASP, MATLAB or Microsoft Office Excel. Significance levels are indicated as follows: $0.1 > \#P > 0.05$; $*P < 0.05$; $**P < 0.01$; $***P < 0.001$; $****P < 0.0001$. No statistical methods were used to predetermine sample size, but it is comparable to previously published work[29,72,73].

Acknowledgements

We thank Z.J. Huang and László Acsády for providing us transgenic mice, Tamás Herczeg, Réka Erdős, Anna Fehér, and Katalin Varga for laboratory assistance, Csaba Dávid and Ákos Babiczky for advising us on axonal analysis and Gábor Nyíri for sharing primary antibodies. We thank Tallie Z. Baram, Antoine Adamantidis and Nadia Urbain for comments and discussions about the manuscript. We also thank the Institute of Enzymology of the Research Centre for Natural Sciences for the use of Zeiss microscope and we would like to thank the Light Microscopy Center of Institute of Experimental Medicine. This work was supported by the Ministry of Innovation and Technology of Hungary from the National Research, Development and Innovation Fund (K138836, and KKP126998 to FM; FK135285, FK144583 to SB; PD124034 to BB), by the Hungarian Brain Research Program (2017-1.2.1-NKP-2017-00002 to FM; NAP2022-I-7/2022 to MLL) by the New National Excellence Program of the Ministry for Innovation and Technology (ÚNKP-21-5-ÁTE-2 to FM; ÚNKP-22-2-III-ELTE-539 to AVB, ELKH SA-48/2021), by Cooperative Doctoral Program (KDP-2020-1015461 to

AM), by supported by the new national excellence program of the ministry for culture and innovation from the source of the national research, development and innovation fund (EKÖP-2024-87 to PB, EKÖP-2024-276 to AVB). FM was a János Bolyai Research Fellow.

Contributions

A.M., P.B., B.B. and F.M. conceived and designed the project. A.M., P.B., B.B., A.V.B. and F.M. performed experiments. A.M., P.B., S.B. and F.M. analysed data. A.M., P.B., M.L.L. and F.M. prepared figures and wrote the manuscript. The other authors made valuable comments on drafts of the manuscript and figures. S.B., M.L.L and F.M. supervised electrophysiology experiments. F.M. supervised the entire project.

Data availability

All data that support the findings of this study are available from the corresponding author upon request. Source data are provided with this paper.

Code availability

Custom-written codes used to analyze data from this study are available from the corresponding author upon request.

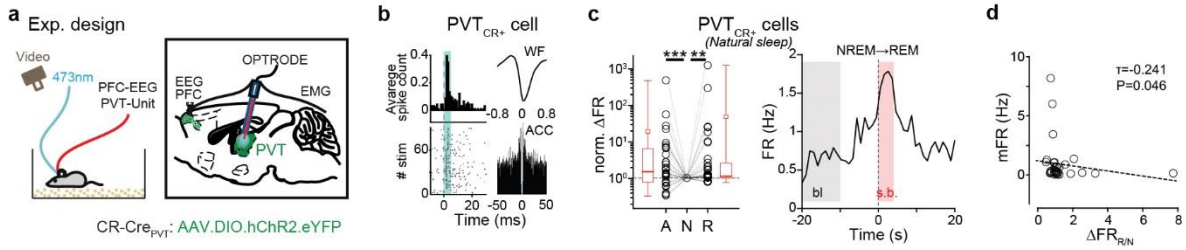

Fig. 1: PVT activity displays sleep stage-dependent activity

a, Schematic of natural sleep recordings from PVT using an optrode in Calb2 (CR)-Cre mice. **b,** Optogenetic identification (blue) of a PVTCR+ cell. WF, waveform; ACC, autocorrelogram. **c,** Left, normalized activity indicates state-dependent firing rate of PVTCR+ cells (black circles; N= 34 cells, n = 3 animals; Friedman ANOVA with Wilcoxon matched-pairs test). A, awake; N, NREM sleep; R, REM sleep. Right, the averaged REM-linked increase in PVTCR+ activity is particularly present at the NREM-to-REM transition during natural sleeping (also see **Extended Data Fig. 1b,c**; Friedman ANOVA with Wilcoxon matched-pairs test). Pink, 1 s bins with significant elevation (s.b.) compared to baseline (bl, grey). **d,** Negative correlation between mean firing rate (mFR) and REM induced firing rate changes (R/N) of individual PVTCR+ cells (Kendall's TAU Correlations). Box and whisker plots in c indicate median, interquartile range, and squares indicate means. **$P < 0.01$; ***$P < 0.001$. (**Statistics in Extended Data Table 1**).

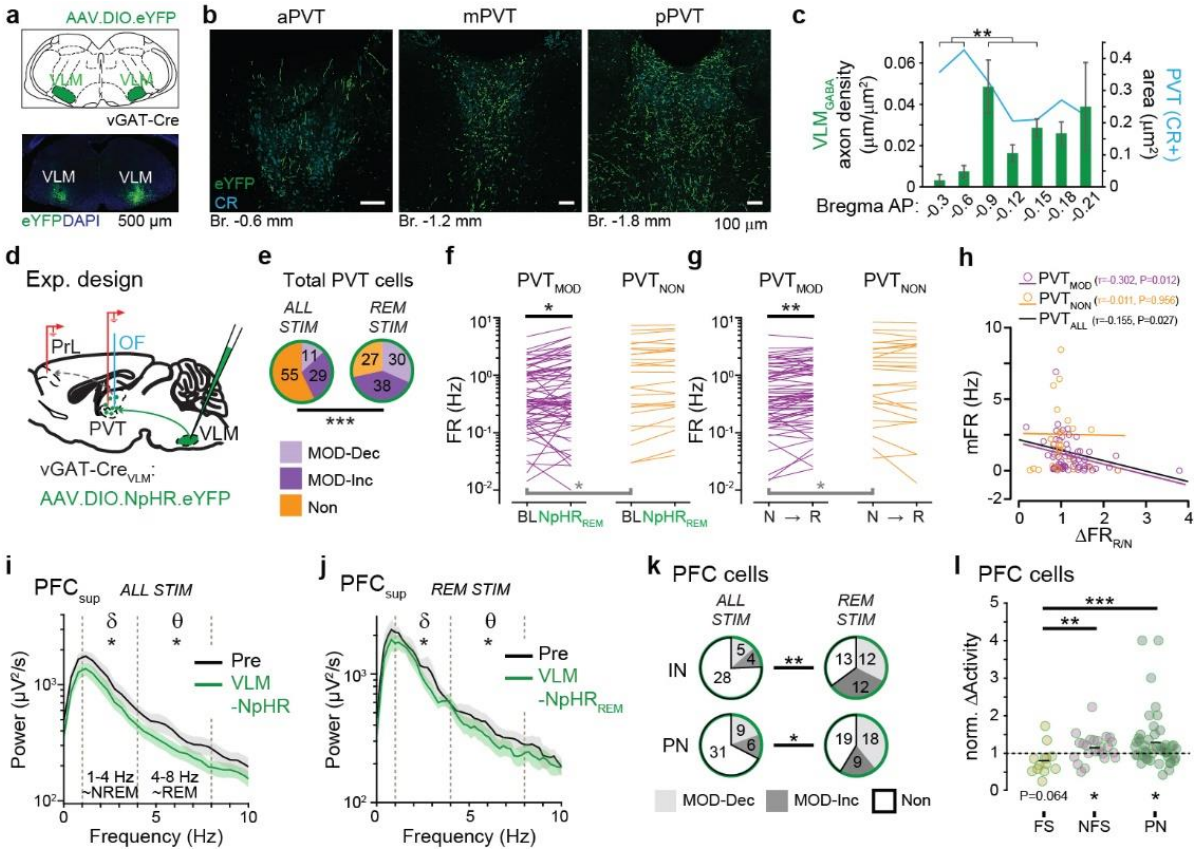

Fig. 2: VLM$_{GABA}$-to-PVT inputs shape REM-related theta oscillation in the superficial PFC

a, Schematic (*top*) of and injection sites (*bottom*) targeting VLM$_{GABA}$ cells in vGAT-Cre mice. **b,** Representative confocal images of eYFP-labeled VLM$_{GABA}$-to-PVT (green) at three anteroposterior levels. Cyan color shows the CR counterstaining indicating territory of PVT. **c,** Quantification of topographic distribution of VLM$_{GABA}$-to-PVT inputs (n = 3 animals; Shapiro-Wilk W test with paired t-test). **d,** Schematic of simultaneous PVT and PFC recordings with optogenetic silencing (NpHr3.0) of VLM$_{GABA}$-to-PVT inputs. **e,** Pie charts showing state-dependent responsiveness of PVT cells (N = 95; n = 7 mice) to inhibition of VLM$_{GABA}$-to-PVT inputs (Pearson's $\chi 2$ test). *ALL STIM*, all trials; *REM STIM*, inhibition during high theta power (~REM) periods. **f,** Baseline (BL) and evoked PVT activity by inhibition of VLM$_{GABA}$-to-PVT inputs during high theta trials (NpHR$_{REM}$) clustered by responsiveness to the inhibition (PVT$_{MOD}$ vs. PVT$_{NON}$) (Wilcoxon matched-pairs test for BL vs. NpHR$_{REM}$; Mann-Whitney U test for PVT$_{MOD}$ vs. PVT$_{NON-MOD}$). Black asterisk, significant changes of PVT$_{MOD}$ (N=68 cells) upon inhibition; grey asterisk, significant difference between baseline firing of PVT$_{MOD}$ and PVT$_{NON}$ (N=27 cells). **g,** Firing rate changes upon NREM (N)-to-REM (R) transition were observed only in PVT$_{MOD}$ cells (Wilcoxon matched-pairs test for NREM vs. REM; Mann-Whitney U test for PVT$_{MOD}$ vs. PVT$_{NON}$). Grey asterisk, significant difference between NREM firing of PVT$_{MOD}$ and PVT$_{NON}$. **h,** Negative correlation between mean firing rate (mFR) and REM-induced firing rate changes (R/N) observed only in PVT$_{MOD}$ cells (Kendall's TAU Correlations). **i,j,** FFT changes of LFP responses to inhibition of VLM$_{GABA}$-to-PVT inputs (green) in superficial PFC layers (PFC$_{sup}$) relative to pre-stim (black) in *ALL STIM* (**i**) and in *REM* STIM trials (**j**) (n = 7 animals; Wilcoxon matched-pairs test). (For quantifications, see **Extended Data Fig. 2c,f.**) **k,** Pie charts showing state-dependent responsiveness of PFC IN (N = 37 cells) and PN cells (N = 46 cells) to the inhibition of VLM$_{GABA}$-to-PVT inputs (n = 7

animals; Pearson's $\chi 2$ test). **l,** Normalized activity changes of FS (N = 13 cells), NFS (N= 24 cells) and PN PFC cells evoked by the inhibition of VLM_{GABA}-to-PVT inputs during high theta (REM-like) states (Wilcoxon matched-pairs test for Pre-stim vs. $NpHR_{REM}$; Mann-Whitney U test for FS vs. NFS vs. PN). Data in **c** and **i,j** are mean ± s.d, in **l** individual data points and means. *P < 0.05; **P < 0.01; ***P < 0.001. (Statistics in **Extended Data Table 1**).

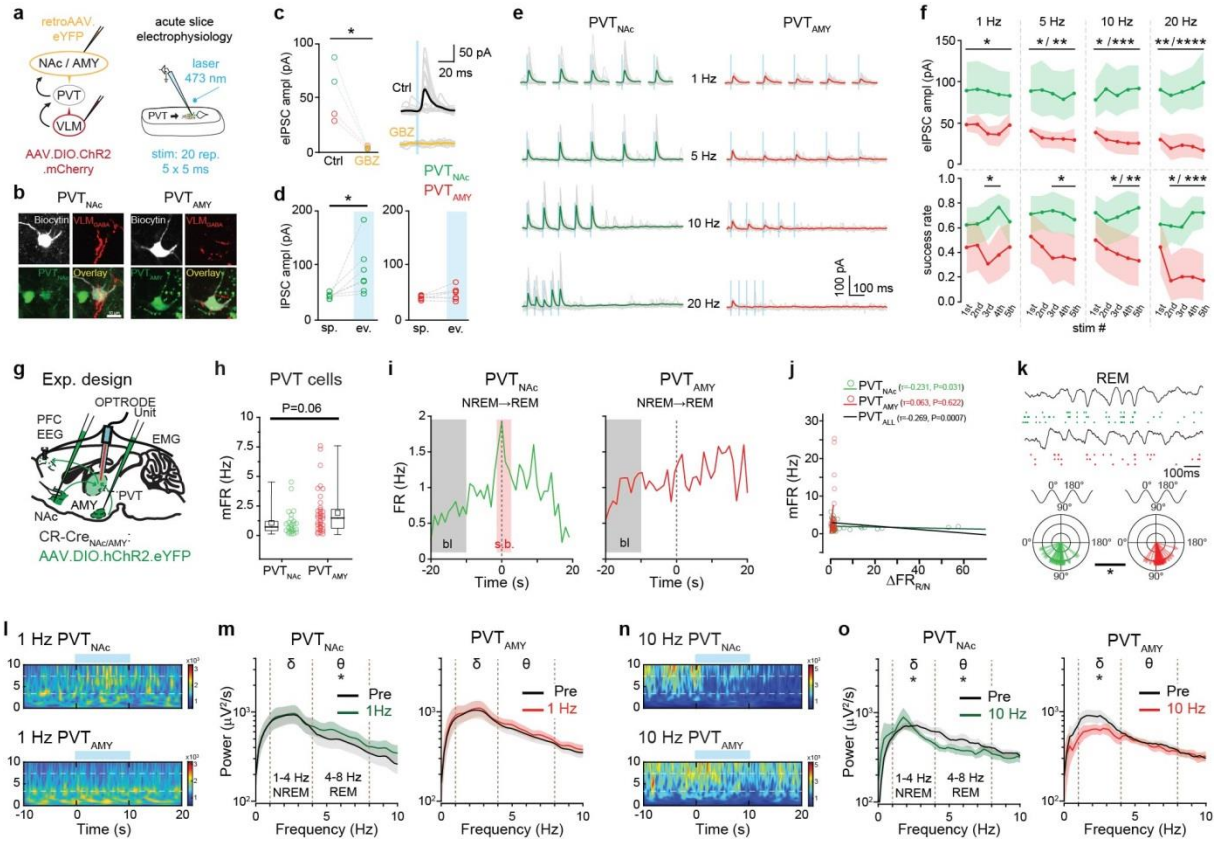

Fig. 3: PVT_{NAc} neurons mediate VLM_{GABA} effects on prefrontal cortical REM sleep
a, Schematic of slice electrophysiology in PVT of vGAT-Cre mice examining VLM_{GABA} inputs onto projection-specific PVT cells. **b,** Representative high-magnification Z-stack confocal images (3 µm total in depth) showing biocytin-filled (white), PVT_{NAc} (green; *left*) and PVT_{AMY} (green; *right*) cells contacted by VLM_{GABA} inputs (red). **c,** *Left*, optogenetically evoked GABAergic IPSCs (eIPSC; Ctrl) in PVT cells (N = 4) were completely abolished by gabazine (GBZ; orange). *Right*, example traces of a PVT_{NAc} cell in Ctrl (black) and GBZ (orange) conditions (Student's t-test). **d,** Population data for spontaneous and evoked IPSCs of PVT_{NAc} (green) and PVT_{AMY} cells (red; N = 7-7; Student's t-test). **e,** Example traces of a PVT_{NAc} and PVT_{AMY} cell for frequency-dependent eIPSCs. **f,** Population data for eIPSC amplitude and success rate (One-Way ANOVA, Bonferroni's post hoc comparisons). **g,** Schematic of in vivo recordings of PVT_{NAc} or PVT_{AMY} cells during natural sleep. **h,** Difference in mean firing rate (mFR) of PVT_{NAc} (N = 25 cells; n = 7 animals) or PVT_{AMY} cells (N = 36 cells; n = 8 animals; Mann-Whitney U test). **i,** Elevation in mean firing rate at NREM-to-REM transition for PVT_{NAc} (*left*) but not PVT_{AMY} cells (*right*; Wilcoxon matched-pairs test). Pink color, 1 s bins with significant elevation (s.b.) compared to baseline (bl, grey). **j,** Negative correlation between mean firing rate (mFR) and REM induced firing rate changes (R/N) restricted to PVT_{NAc} cells Kendall's TAU Correlations). **k,** Distinct phase-locked firing of PVT_{NAc} (green) and PVT_{AMY} cells (red) during REM-associated theta oscillation (Pearson's $\chi 2$ test). *Top*, example unit activity of a PVT_{NAc} (green) and PVT_{AMY} cell (red). *Bottom*, vector diagram of population data. **l-o,** Frequency-dependent bidirectional effects of optogenetic stimulation of PVT_{NAc} and PVT_{AMY} on REM-associated theta oscillation indicated by wavelets (**l,n**) and FFT changes (**m,o**) (n = 7-8 mice; Wilcoxon matched-pairs test). (For quantifications, see **Extended Data Fig. 5e,f.**) Data in **c**-*right*,**e** are individual data points and means, and in **f,m,o** means ± SD. Box and whisker plots in **h** show median, interquartile range, and squares indicate means. *P < 0.05; **P < 0.01; ***P < 0.001; ****P < 0.0001. (Statistics in **Extended Data Table 1**).

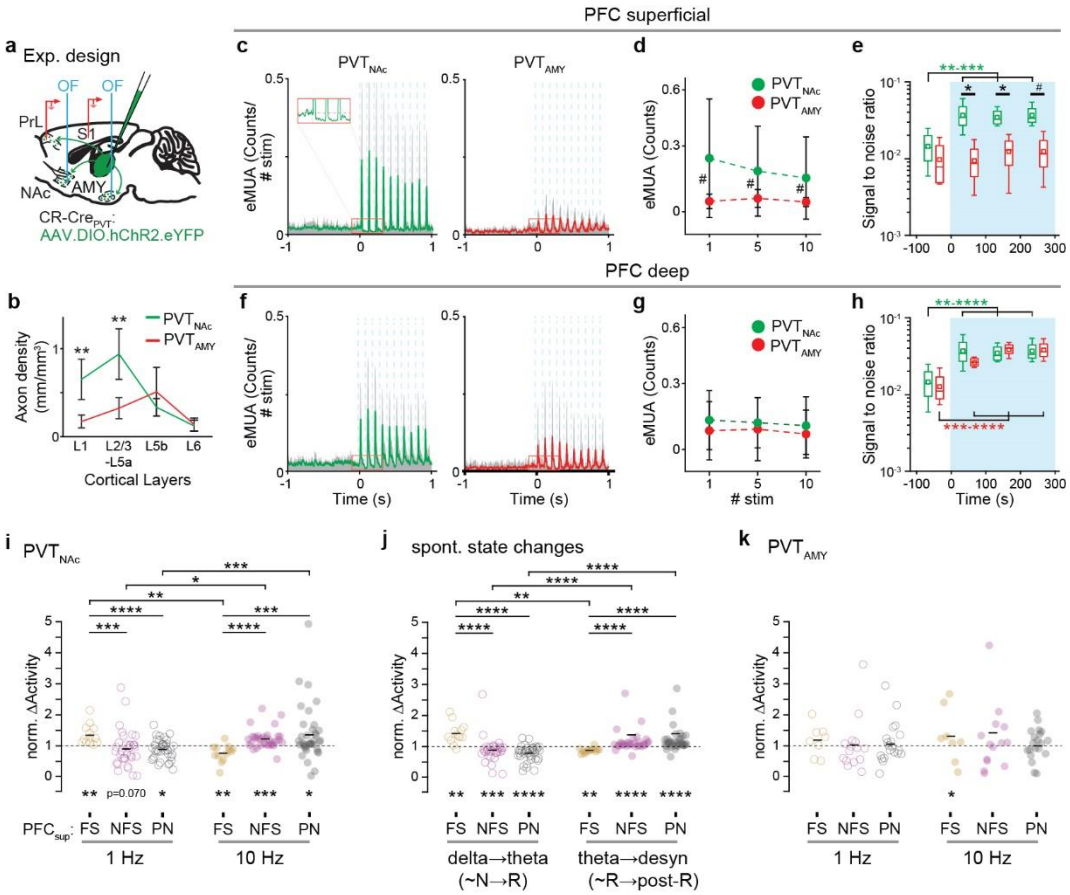

Fig. 4: Frequency-dependent and layer-specific effects of PVT_{NAc} on PFC circuit underlying modulation of theta oscillation

a, Schematic of anesthetized recordings investigating the effects of PVT_{NAc} or PVT_{AMY} activation on PFC circuit. **b,** Distinct, layer-specific distribution of PVT_{NAc} and PVT_{AMY} inputs in PFC (One-way ANOVA with post hoc LSD test). **c-h,** Distinct, layer-specific effects of PVT_{NAc} and PVT_{AMY} activation in PFC. Representative cases for evoked multiunit activity (eMUA) in the superficial (**c**) and deep layers of PFC (**f**); population data for eMUA (**d, g**; n= 4 mice; Wilcoxon matched-pairs test); population data for signal-to-noise ratio of eMUA (**e, h**; n=4 mice; Repeated Measures ANOVA with post hoc LSD test). **i,** Opposite activation of PFC FS (N=13 cells), NFS (N= 33 cells) and PN (N= 37 cells) triggered by 1 Hz and 10 Hz activation of PVT_{NAc} (n=7 mice; Wilcoxon matched-pairs test for baseline vs 1 Hz vs. 10 Hz; Mann-Whitney U test for FS vs. NFS vs PN). **j,** Similar shifts in PFC FS, NFS and PN activation at spontaneous state changes: from high delta periods to high theta periods (similar to NREM (N) → REM (R)) and from high theta periods to desynchronized state (similar to REM (R) → post-REM (R)) (respectively) (n=7 mice; Wilcoxon matched-pairs test for delta→theta vs. theta→desyn; Mann-Whitney U test for FS vs. NFS vs. PN). **k,** PVT_{AMY} stimulation did not elicit state-dependent activation of PFC FS, NFS and PN (n=7 mice; Wilcoxon matched-pairs test for baseline vs 1 Hz vs 10 Hz; Kruskal-Wallis ANOVA for FS vs. NFS vs. PN). Data in **b-d,f,g** means ± s.d and in **i-k** individual data points and means. Box and whisker plots in **e,h** indicate median, interquartile range, and squares indicate means. *$P < 0.05$; **$P < 0.01$; ***$P < 0.001$; ****$P < 0.0001$. (Statistics in **Extended Data Table 1**).

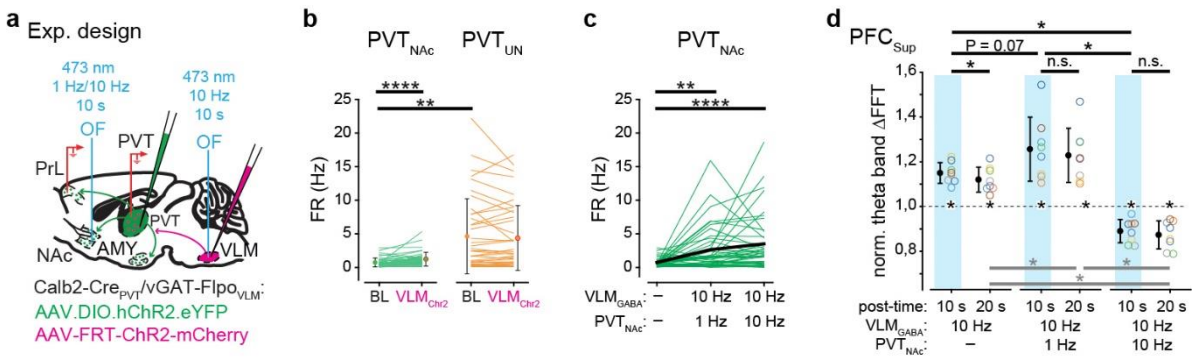

Fig. 5: PVT$_{NAc}$ bidirectionally modulate the VLM$_{GABA}$ effects on theta oscillation in a frequency-dependent manner

a, Schematic of anesthetized recordings investigating the effects of PVT$_{NAc}$ and VLM$_{GABA}$ optogenetic co-activation. **b,** Baseline (BL) and evoked PVT activity by stimulation of VLM$_{GABA}$ neurons clustered by responsiveness to the antidromic phototagging from NAc (PVT$_{NAc}$; N=41 cells) vs. PVT$_{UN}$ (N= 39 cells; n=8 mice; Wilcoxon matched-pairs test for BL vs. VLM$_{ChR2}$; Mann-Whitney U test for PVT$_{NAc}$ vs. PVT$_{UN}$). **c,** Baseline (BL) and evoked PVT$_{NAc}$ activity by paired stimulation of VLM$_{GABA}$ and PVT$_{NAc}$ at 1 and 10 Hz (Wilcoxon matched-pairs test). **d**, Frequency-dependent bidirectional effects of paired stimulation of PVT$_{NAc}$ and VLM$_{GABA}$ on REM-associated theta oscillation (Wilcoxon matched-pairs test). Data in **b, d** means ± s.d and in **n** individual data points and means. *P < 0.05; **P < 0.01; ****P < 0.0001. (Statistics in **Extended Data Table 1**).

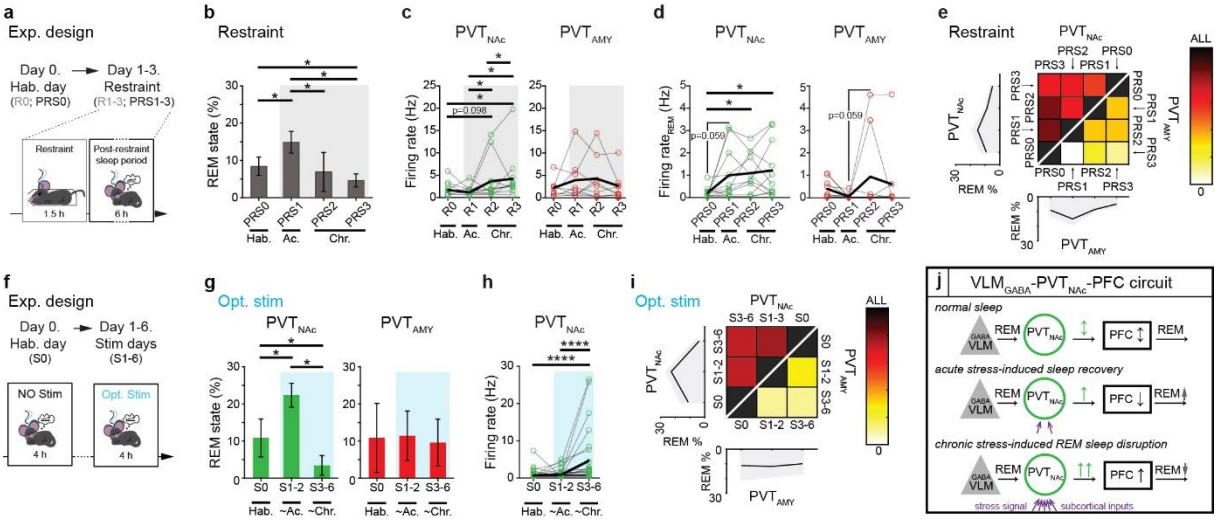

Fig. 6: Stress-induced bidirectional modulation of REM sleep by PVT_{NAc} neurons
a, Schematic of behavioral condition for investigating stress-dependent REM sleep changes. **b,** Acute (Ac.) and chronic (Chr.) restraint induced REM state changes during post-restraint sleep periods (PRS1-3) compared to habituation day (Hab.; PRS0) (n = 6 mice; Wilcoxon matched-pairs test). **c,d,** Population data for restraint induced activity changes of PVT_{NAc} (*left*; N = 11 cells) and PVT_{AMY} cells (*right*; N = 9 cells) during restraint (R0-R3; **c**) and post-restraint REM sleep periods (PRS0-PRS3; **d**) (Repeated Measures ANOVA with post hoc LSD test). **e,** Heat map indicating the number of thalamic cells with restraint induced elevated activity compared to previous days, together with REM state changes (same as in **b**). **f,** Schematic of behavioral condition for investigating optogenetic activation of PVT_{NAc} (n = 7 mice) and PVT_{AMY} neurons (n = 8 mice) induced REM sleep changes. **g,** Optogenetic stimulation (blue) of PVT_{NAc} (*left*) but not PVT_{AMY} (*right*) triggered similar REM state changes as acute and chronic restraint stress (Friedman ANOVA with Wilcoxon matched-pairs test). **h,** Population data indicate increase in PVT_{NAc} activity (N = 25 cells) during non-stim periods (Repeated Measures ANOVA with post hoc LSD test). **i,** Heat map indicating the number of cells (PVT_{NAc} N = 25 cells; PVT_{AMY} N= 36 cells) with elevated activity compared to previous days, together with the corresponding PVT_{NAc}- and PVT_{AMY}-induced REM state changes (same as in **g**). **j,** Summary diagram indicates PVT_{NAc}-mediated REM sleep changes alterations in normal and stressful conditions. Data in **b,g**, means ± SD. Thick black lines in **c,d,h** indicate mean. *$P < 0.05$; **$P < 0.01$; ****$P < 0.0001$. (Statistics in **Extended Data Table 1**).